ICARUS 110, 79–94 (1994)

Radio Occultation Studies of the Venus Atmosphere with the Magellan Spacecraft

2. Results from the October 1991 Experiments

JON M. JENKINS

SETI Institute/NASA Ames Research Center, MIS 244-11, Moffett Field, California 94035-1000
E-mail: jenkins@nova1.stanford.edu

PAUL G. STEFFES

School of Electrical and Computer Engineering, Georgia Institute of Technology, Atlanta, Georgia 30332-0250

AND

DAVID P. HINSON, JOSEPH D. TWICKEN, AND G. LEONARD TYLER

Center for Radar Astronomy, Stanford University, Stanford, California 94305-4055

Received October 20, 1993; revised March 28, 1994

On October 5 and 6, 1991, three dual-frequency ingress radio occultation experiments were conducted at Venus during consecutive orbits of the Magellan spacecraft. The radio signals probed a region of the atmosphere near 65°N, with a solar zenith angle of 108°, reaching below 35 km at 3.6 cm, and below 34 km at 13 cm (above a mean radius of 6052 km). The high effective isotropic radiated power (EIRP) of the Magellan spacecraft and highly successful attitude maneuvers allowed these signals to probe deeper than any previous radio occultation experiment and also resulted in the most accurate thermal and sulfuric acid vapor abundance profiles ever obtained at Venus through radio occultation techniques. The performance of the spacecraft and the experiment design are discussed in an accompanying paper by P. G. Steffes, J. M. Jenkins, R. S. Austin, S. W. Asmar, D. T. Lyons, E. H. Seale, and G. L. Tyler (1994, *Icarus* 110, 71–78). Average electron density profiles retrieved from the data possess peaks between 2600 and 6000 cm^{-3}, well below typical values of 10,000 cm^{-3} retrieved in 1979 by Pioneer Venus at similar solar zenith angles. Other basic results include vertical profiles of temperature, pressure, and density in the neutral atmosphere, 13- and 3.6-cm absorptivity, and H_2SO_4(g) abundance below the main cloud layer. H_2SO_4(g) becomes significant below 50 km, reaching peaks between 18 and 24 ppm near 39 km before dropping precipitously below 38 km. These sharp decreases confirm the thermal decomposition of sulfuric acid vapor below 39 km. Since the Venus atmosphere rotated approximately 10° between experiments, the data contain information about the horizontal variability of the atmosphere. All derived profiles exhibit significant variations from orbit to orbit, indicating the presence of dynamical processes between 33 and 200 km. In particular, the orbit-to-orbit variations in temperature and in H_2SO_4(g) abundance appear to be correlated, suggesting that a common mechanism may be responsible for the observed spatial variations.

1. INTRODUCTION

The Magellan spacecraft has distinguished itself through its success at mapping the surface and the gravity field of Venus (Saunders 1992). For several reasons, Magellan is also an excellent platform for conducting radio occultation experiments of the Venus atmosphere (Steffes *et al.* 1994). Due to its high effective isotropic radiated power (EIRP) and its maneuverability, Magellan is capable of probing the atmosphere of Venus to within 1 km of the theoretical limit of 33 km at both 13-cm (2.29 GHz or *S*-band) and 3.6-cm (8.36 GHz or *X*-band) wavelengths. To date, nine dual-frequency radio occultation experiments have been conducted with the Magellan spacecraft: three experiments in October 1991 and six experiments in December 1992. While radio occultation studies of Venus have been conducted with several other spacecraft, none

0019-1035/94 $6.00

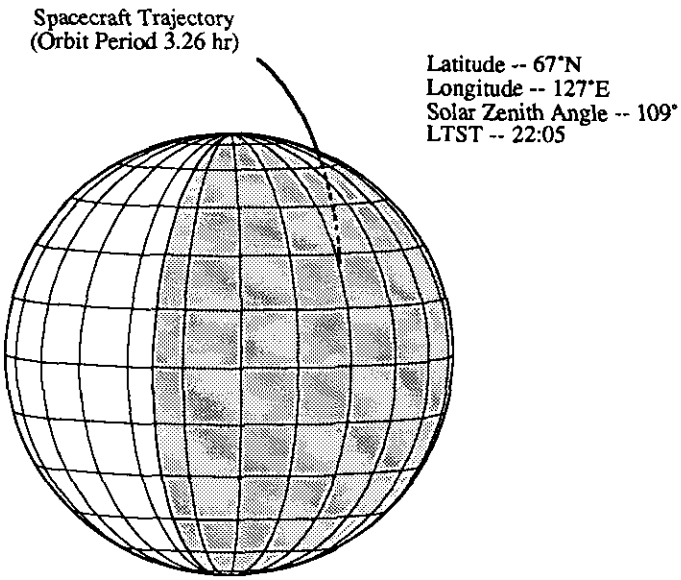

FIG. 1. The trajectory of Magellan during the occultations presented here, as viewed from Earth. The spacecraft arced over the northeastern limb of Venus and passed behind the limb as the experiment progressed. Large atmospheric refractivity bent the radio signal from the spacecraft around the limb, so that the communication link continued until Magellan was well behind the planet, as seen from Earth. The morning terminator and dark side of Venus are visible in this diagram. Longitude lines are placed every 15° and latitude lines are spaced 15° apart.

have penetrated the atmosphere as deeply, or retrieved profiles with smaller uncertainties than Magellan (Steffes *et al.* 1994). In addition, the availability of data at both 13 and 3.6 cm makes it possible to place limits on the abundance of another important sulfur-bearing gas, sulfur dioxide (SO_2), as well as to derive abundance profiles of sulfuric acid vapor (H_2SO_4). This paper describes the results of the three ingress occultation experiments conducted on successive orbits on October 5 and 6, 1991. The results from the experiments conducted in December 1992 will be reported in future publications.

These experiments probed the neutral atmosphere at altitudes between 33 and 100 km. Figure 1 shows the experiment geometry, which was nearly identical for all three occultations. (The only significant difference in experiment geometry among the three orbits was due to the 5-day rotation of the atmosphere of Venus.) The angle between the spacecraft orbit plane and the direction to Earth at the time of the measurements was about 28°, so that the occultations were nondiametric. Hence, during each experiment, the ray paths followed by the radio signals sliced obliquely through the atmosphere. In traversing the range of altitudes given above, the proximate point, or point of closest approach to Venus along the ray path, sampled latitudes from 68°N to 56°N, longitudes from 128°E to 139°E, and solar zenith angles from 109° to 114°. The direction along the ray path near the proximate point nearly coincided with the local east–west direction on Venus (it varied between 280° and 290° from North during each experiment.)

The data products from the radio occultation experiments include average electron density in the ionosphere; temperature, pressure, and density in the neutral atmosphere; 13- and 3.6-cm absorptivity profiles; vertical profiles of the abundance of $H_2SO_4(g)$; and constraints on the abundance of $SO_2(g)$. In addition, uncertainties have been placed on these profiles using the standard propagation of errors (Brandt 1963). We obtained these results by following a standard sequence of steps for inverting radio occultation data, supplemented by the use of optimal digital filters for producing the absorptivity and $H_2SO_4(g)$ abundance profiles (Jenkins 1992). In addition, we developed a new method for analyzing two-way radio occultation experiments that yields extract results in the absence of noise. Other methods, which place *a priori* constraints on the solution, introduce systematic errors which would have been larger than the stochastic errors for these data sets. (Appendix A describes the new method in depth and compares it to previous methods.) Future laboratory measurements and theory should improve the accuracy of the expression for the absorptivity due to $H_2SO_4(g)$ at 3.6 cm. This will allow abundance profiles of $SO_2(g)$ to be determined from these data sets, rather than just upper limits. Since the atmosphere of Venus rotates about 10° during each 3.26-hr orbit of the spacecraft, these data also make it possible to investigate zonal variations in the Venus atmosphere.

2. DATA ANALYSIS

This section begins with a brief description of the experiment and the steps taken to process and analyze the data. Because most of the steps are routine and well-documented in the literature (e.g., Fjeldbo and Eshleman 1968, Lipa and Tyler 1979, Jenkins and Steffes 1991, and Jenkins 1992), only the aspects which are unique to the treatment of these data sets are emphasized.

The raw data sets consisted of open-loop recordings of the 13- and 3.6-cm carrier signals received at DSN Station 43[1] at Tidbinbilla, Australia, along with spacecraft trajectory and planetary ephemerides information, supplied by JPL Navigation and the Magellan Project, and reconstructions of the actual limb-tracking maneuvers executed by the spacecraft, supplied by Martin Marietta Corporation. The "open-loop" recordings contained four channels digitized at 8 bits and samples at 50 kHz: 13-cm right-hand circular polarization (RCP), 13-cm left-hand circular polarization (LCP), 3.6-cm RCP, and 3.6-cm LCP. The bandwidths of the receivers were 20 kHz prior to sampling.

[1] The 70-m-diameter antenna of the NASA Deep Space Network.

Since Magellan transmits in linear polarization at 13 cm, the 13-cm RCP and LCP signals each contained half the power received at the ground station. At 3.6 cm, Magellan transmits RCP, so that the 3.6-cm signal of primary interest was the RCP channel.

Obtaining thermal profiles and abundance profiles of H_2SO_4(g) from the raw data sets requires several steps. First, the open-loop recordings were processed to obtain time-series of frequency and power (log intensity) for each channel. The frequency time-series were used to determine the 13- and 3.6-cm refractivity profiles, from which the electron density, temperature, pressure, and density profiles were derived. The power time series, in conjunction with the frequency time series, were used to derive 13- and 3.6-cm absorptivity profiles. These were combined with the temperature/pressure profiles to obtain abundance profiles of H_2SO_4(g) and constraints on the abundance of SO_2(g). These steps are described in more detail below.

A. Preprocessing the Open-Loop Recordings

Standard digital signal processing techniques were applied in order to filter and reduce the bandwidth of the signals recorded at the DSN by a factor of 16. Care was taken to ensure that none of the signals drifted outside of the passband of the filter applied prior to decimation. Next, the signals were "steered" to the center of the band. This entailed mixing each signal with a time-varying complex sinusoid of unit amplitude whose phase varied in a manner opposite to that expected for the observed signal, based on the occultation geometry, the manner in which the baseband center frequencies at the DSN were slewed during the experiments, and a model atmosphere derived from initial processing of the data. This step ensured that the instantaneous frequency of each signal changed slowly over time, so that the frequency and intensity of the steered signals could be determined more accurately.

The method of Lipa and Tyler (1979) was used to generate estimates of the intensity and frequency of each signal as time series, as well as to estimate the uncertainties in power and frequency. This method assumes that the signal is well-modeled as a quasi-stationary sinusoid in white Gaussian noise (WGN). However, the carrier signals were so strong at the beginning of each occultation that the phase noise of the Magellan transmitter was well above the noise floor (preimmersion carrier to noise ratios, or CNRs, were approximately 60 dB for the RCP 3.6-cm signal, and 48 dB for both 13-cm channels). This caused the algorithm to underestimate the magnitudes of the errors in frequency at the beginning of each experiment until the phase noise dropped below the noise floor as the occultation progressed. To correct for this effect, we constructed error estimates from the time series themselves by taking the root mean square error of sliding seven point fits to quadratic polynomials. This alternate method produced good error estimates during the free space portion of the signals, but tended to overestimate the errors in the vicinity of frequency and power fluctuations caused by small-scale structure in the refractivity profile of the atmosphere. It was possible to match the empirical frequency variance estimates in the free-space portion of the measurements by raising the original 3.6-cm estimates to the power 2/3, and the original 13-cm frequency variance estimates to the power 5/6.

Three block sizes were used to produce time series with sampling periods of 0.0819, 0.1638, and 0.3277 sec. All profiles reported here were inferred from time series with a sampling period of 0.1638 sec. The sampling period of 0.1638 sec provided a compromise between the smaller period, which provided greater vertical resolution, and the longer period, which was less sensitive to thermal measurement noise and, hence, produced longer usable time series with smaller stochastic errors, but with coarser vertical resolution. The 13-cm RCP and LCP frequency and intensity time series were averaged together for each experiment, to reduce the noise fluctuations. This reduced the errors on the resulting 13-cm data sets by a factor of $\sqrt{2}$ since the errors on each of the channels were uncorrelated. (An attempt was made to coherently detect and estimate the intensity and frequency of the 13-cm LCP and RCP signals. This task, however, was made quite difficult since the spacecraft rolled approximately 10° during each maneuver, causing the phase difference between the RCP and LCP channels to vary continuously during the measurements.) The LCP and RCP 3.6-cm power profiles were compared in order to search for depolarization events that may be indicative of lightning events (Furuta *et al.* 1985). No such depolarization events were detected, however, and the LCP 3.6-cm signals were then abandoned, since they could not be usefully incorporated into the RCP 3.6-cm data set.

For the purposes of investigating the neutral atmosphere, the effects of the ionosphere of Venus and the interplanetary plasma were removed to first order from the data sets by using the differential Doppler shift between the 13-cm and the 3.6-cm signals. (Refractivity of the ionospheric plasma is a strong function of frequency, unlike the case for the neutral atmosphere of Venus.) This correction was made over an interval in each data set where the differential Doppler shift was significant so that the errors in the resulting data sets were uncorrelated outside this limited interval. Similarly, a differential Doppler data set was created to study the Venus ionosphere by combining the 13- and 3.6-cm frequency time series. This produced a frequency time series without the effects of the neutral atmosphere.

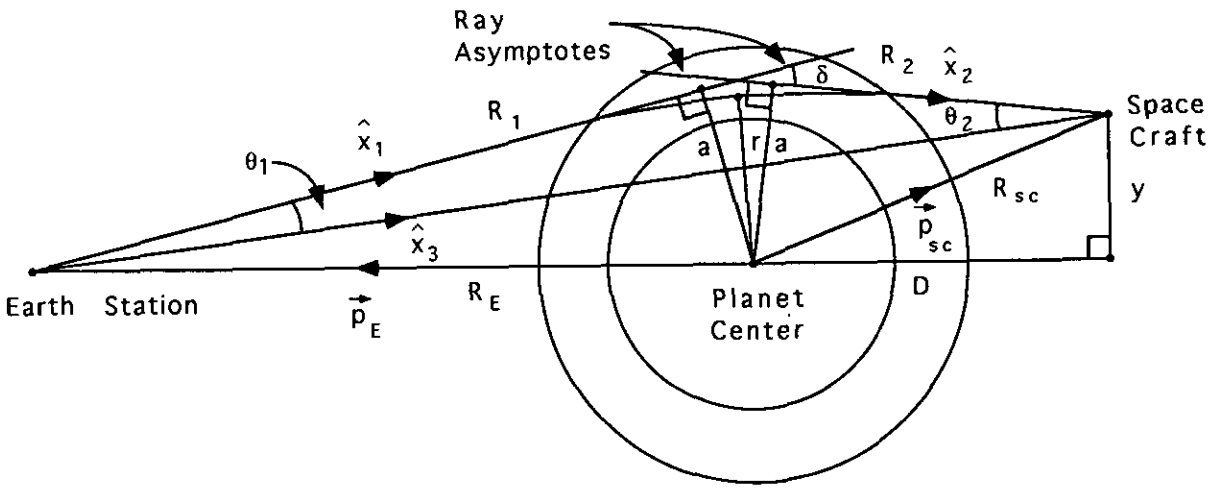

FIG. 2. Occultation experiment geometry. The geometry is shown for the downlink leg of a two-way radio occultation experiment. Positions and rays apply at the appropriate event times.

B. Analyzing the Frequency Time Series

The Magellan radio occultation experiments were conducted in the two-way mode (i.e., the same as is used to collect tracking data for spacecraft navigation). A stable reference signal at frequency f_t = 2.1 GHz is uplinked to the spacecraft from the Earth station. The spacecraft locks its oscillator to the frequency f_{SC} of the signal received and downlinks two signals, one at a frequency of (240/221) f_{SC} (i.e., 13 cm) and a second at a frequency (240/221)(11/3)f_{SC} (i.e., 3.6 cm). These multiplicative constants are determined by hardware onboard the spacecraft. All signals are unmodulated throughout the experiment. The power output of the spacecraft is stabilized internally. The Earth receiving station records the signals transmitted by the spacecraft as it passes behind the limb of Venus as viewed from Earth (cf. Fig. 1).

Figure 2 shows the experiment geometry and defines parameters. The frequency of the signal received during a radio occultation, $f_r(t)$, experiences a Doppler shift due to the relative motion between the source and receiver along the actual ray path. Because the ray path is deflected by an angle δ due to atmospheric refraction, this Doppler shift differs from what would have been observed if no atmosphere were present. It is important to note that for two-way experiments, each ray passes twice through the Venus atmosphere: once on the uplink path from the ground station to the spacecraft and again on the downlink from the spacecraft that is received and recorded at the ground station two light times later (about 8 min for these experiments). Thus, the observed frequency shift from the free space value is determined by the geometry of both the uplink and the downlink ray paths traveled by a particular wave front.

The bending angle, $\delta(t)$, and ray impact parameter, $a(t)$, of the downlink ray path were determined from the received frequency, $f_r(t)$, and the positions and velocities of the spacecraft and the ground station relative to Venus. The ray path parameters were solved for using a method that does not rely on *a priori* assumptions, unlike previous methods. Appendix A contains a thorough discussion of the difficulties involved in solving for these parameters in the case of a two-way radio occultation experiment, and describes the method used here. The index of refraction $n(a)$ was found by applying the following Abel-type transform to the ray path parameters,

$$\log_e(n(r)) = \frac{1}{\pi}\int_a^\infty \frac{\delta(x)dx}{\sqrt{x^2 - a^2}}, \tag{1}$$

where r is the radius of closest approach, or the proximate point, for the ray with impact parameter a. The integral extends over all measured impact parameters such that $x \geq a$. The relationship between r and a is given by

$$r = \frac{a}{n}. \tag{2}$$

This relationship between the index of refraction of a spherically symmetric medium and parameters defining ray asymptotes for light rays traversing the medium was derived by Fjeldbo *et al.* (1971).

Since the bulk of the neutral atmosphere of Venus is composed of nonpolar gases (carbon dioxide (CO_2) and molecular nitrogen (N_2)), and is well-mixed, the density of the atmosphere $\rho(r)$ is related to the refractivity $N \equiv (n - 1) \times 10^6$ by a scalar multiple, which is 3.9827 ×

10^{-3} kg/m^3 for an atmosphere composed of 96.5% CO_2 and 3.5% N_2, (refractivity values from Essen and Froome 1951). Then, assuming that the atmopshere is in hydrostatic equilibrium,

$$P(r) = \rho(r_0) RT_0 + \int_r^{r_0} \rho(y) g(y)\, dy \tag{3}$$

and

$$T(r) = \frac{P(r)}{\rho(r)R} = \frac{\rho(r_0)}{\rho(r)} T_0 + \frac{\int_r^{r_0} \rho(z) g(z)\, dz}{\rho(r)R}, \tag{4}$$

where r_0 is the top of the sensible atmosphere, R is the gas constant, ρ is the density in kg/m^3, g is the acceleration of gravity in m/s^2, P is pressure in Pascal, and T is temperature in Kelvin, and T_0 is the assumed boundary temperature at r_0 (Lipa and Tyler 1979). We chose r_0 to be that level in the atmosphere where the standard deviation in refractivity was 1/10th of the estimated value. This represents a tradeoff between the desire to carry the integration as high as possible and the desire to limit the effect of noise fluctuations on the temperature profiles. It is clear that one must choose a boundary condition at r_0 in terms of either temperature or pressure, which introduces some additional uncertainty. We used values reported by Seiff (1983) for the temperature at radius r_0.

Deriving electron density profiles $n_e(r)$ from the frequency time series corrected for the effects of the neutral atmosphere is more straightforward,

$$n_e = -\frac{2\pi(n-1)}{r_e \lambda^2} \tag{5}$$

where $r_e = 2.82 \times 10^{-15}$ m, and λ is the freespace wavelength of the radio signal (Eshelman 1973).

C. *Analyzing the Power Time Series*

In addition to deriving vertical profiles of temperature, pressure, and density, we also derived vertical profiles of 13- and 3.6-cm absorptivity and abundance profiles of H_2SO_4(g) from the data sets. These tasks required the amplitude time series as well as the frequency time series of the signals and were much more difficult than generating the state parameters. For this discussion, we note that the power, p of a sinusoidal signal is related to the intensity, I and amplitude, A by

$$p = 10 \log_{10}(I) = 10 \log_{10}\left(\frac{A^2}{2}\right) dB. \tag{6}$$

The units of intensity and amplitude are not of much importance since we are interested in the behavior of the power received during the occultation relative to the power received prior to occultation. There are three factors that affect the signal intensity during occultations: refractive defocusing, antenna pointing, and absorption (and scattering) in the atmosphere. Thus, the power profile is the sum of the three terms,

$$p(r) = -\tau(r) + p_{ant}(r) + p_n(r), \tag{7}$$

where τ is the excess attenuation due to absorption (and scattering) in the atmosphere, p_{ant} is the power drop due to mispointing of the antenna, and p_n is the power drop due to refractive effects.

Refractive defocusing is caused by the gradient in refractivity with respect to radius. This distorts the shape of the beam by spreading it in the plane of the occultation (see Fig. 2) and compressing it in the orthogonal direction. The refractive defocusing was estimated from the ray path parameters and the occultation geometry by

$$p_n = 10 \log_{10}\left[\frac{y}{a}\left(1 - R_2 \frac{d\delta}{da}\right)\right] \tag{8}$$

and removed from the power profile (Eshleman *et al.* 1980).

During each of these experiments, maneuvers were executed that attempted to point the spacecraft's high-gain antenna continuously toward the refracted image of Earth. These maneuvers were not perfect, since a model refractivity profile and a predicted spacecraft trajectory were used in their design. This resulted in a peak pointing error of approximately 0.4° during the experiments. The chief contributor to the pointing errors was the use of an orbit prediction generated several months in advance of the experiment. The difference between the actual and designed maneuvers was much smaller, but still measurable at 3.6 cm. Although the effect of these errors on the 13-cm signals was insignificant (<0.4 dB), they resulted in substantial attenuation at 3.6 cm (up to 7 dB). Given the spacecraft maneuver, the occultation geometry, the ray path parameters, and the antenna gain patterns, the power profiles were corrected for this effect by determining the gain of the HGA at 13 and 3.6 cm along the true ray path to Earth.

We found that the 3.6-cm profiles were being overcorrected so that the excess attenuation profiles had significant negative excursions of approximately 2 dB near the start of the maneuver. After consulting members of the Magellan flight team, we determined that the error could be due to a fixed pointing error in the reconstruction of the maneuver, to a small timing error in the execution of

the maneuver, or to inadequate knowledge of the 3.6-cm HGA beam pattern outside the half-power beamwidth. We solved for the combination of a fixed pointing error and a timing error by a least-squares method which attempted to force the 3.6-cm excess attenuation profile to zero prior to any expected significant attenuation due to absorbing gases (CO_2 and H_2SO_4). The timing errors were found to be approximately 1 sec, and the pointing offset was found to be approximately 0.1° for each of the experiments. It should be noted that the range of the excess attenuation at 3.6 cm was over 30 dB, so that this error was small compared to the dynamic range of the measurement, and was confined to that portion of the atmosphere where no significant absorption was detected at 13 cm, or expected at either frequency. Since the error could have been due in part to inadequate knowledge of the 3.6-cm HGA gain patterns, we elected not to apply the new antenna pointing correction to the 13-cm power profiles. (This would not have changed the 13-cm excess attenuation profiles significantly in any event.)

The excess attenuation $\tau(a)$ is related to the absorptivity $\alpha(a)$ through an inverse Abel transform:

$$\tau(a) = 2\int_a^\infty \frac{\alpha(x)dr/da(x)\,x\,dx}{\sqrt{x^2 - a^2}}. \tag{9}$$

Hence, $\alpha(a)$ can be recovered from $\tau(a)$ by multiplying the inverse Abel transform of $\tau(a)$ by the derivative da/dr (a),

$$\alpha(a) = -\frac{da}{dr}(a)\frac{1}{\pi a}\frac{d}{da}\left[\int_a^\infty \frac{\tau(x)x\,dx}{\sqrt{x^2 - a^2}}\right] \tag{10}$$

(Jenkins 1992). Though Eqs. (9) and (10) may seem confusing at first glance, it should be noted that the ray path parameter, a, and the radius of the proximate point, r, can be treated as functions of each other.

The difficulty in determining absorptivity from radio occultation data lies in the necessity to perform one full numerical derivative to estimate the refractive defocusing, one full derivative to compute da/dr, and one inverse Abel transform, which under an appropriate change of variables, is equivalent to performing a half-order derivative (Bracewell 1986). To calculate these parameters, we used a modified version of the Anderssen and Bloomfield spectral differentiator (1974a,b) to compute the necessary derivatives, and a modified version of Anderssen's second method to compute the inverse Abel transform (1976). These techniques exploit the fact that computing a regularized derivative is equivalent to constructing a Wiener filter in the frequency domain if the spectral density of the true data is assumed to take a form represented by a certain parameterized family of power spectra. Jenkins (1992) showed that for simulated radio occultation data, these methods provided more accurate results than alternative methods such as Kalman filtering, linear regression, and simple fixed-point smoothing schemes accompanied by finite difference techniques.

Vertical profiles of the mixing ratio of H_2SO_4(g) were computed for each orbit using the profiles of 13-cm and 3.6-cm absorptivity, temperature, and pressure. First, the absorptivity due to CO_2 (pressure-broadened by CO_2 and N_2) was removed from the absorptivity profiles using the following relation (Ho *et al.* 1966),

$$\alpha_{CO_2}(f) = 1.15 \times 10^8 \left(q_{CO_2}^2 + 0.25 q_{CO_2} q_{N_2} + 0.0054 q_{N_2}^2\right) f^2 P^2 T^{-5}\ \text{dB km}^{-1}, \tag{11}$$

where q is number mixing ratio, f is frequency in GHz, P is pressure in atm, and T is temperature in K. The residual absorptivity is due principally to sulfuric acid vapor (Steffes 1985):

$$\alpha_{H_2SO_4}(13\text{ cm}) = 9.00 \times 10^9\, T^{-3}\, P^{0.50}\, q_{H_2SO_4}\ \text{dB km}^{-1}$$
$$\alpha_{H_2SO_4}(3.6\text{ cm}) = 4.52 \times 10^{10}\, T^{-3}\, P^{0.85}\, q_{H_2SO_4}\ \text{dB km}^{-1}. \tag{12}$$

Another potential microwave-absorbing constituent is SO_2(g), whose absorptivity is given by (Steffes and Eshleman 1982, modified as per Fahd and Steffes 1992):

$$\alpha_{SO_2}(f) = 18 \times 10^6 f^2 P^{1.2} T^{-3.1} q_{SO_2}\ \text{dB km}^{-1}. \tag{13}$$

In theory, it should be possible to solve simultaneously for q_{SO_2} and $q_{H_2SO_4}$ from (12) and (13) given 13- and 3.6-cm absorptivity profiles and temperature and pressure profiles. In practice, however, the expression for 3.6-cm absorptivity for H_2SO_4(g) is not consistent with the radio occultation data. Assuming that no SO_2(g) is present, (12) produces abundance estimates for H_2SO_4(g) from the 3.6-cm data that are much lower than those produced from the 13-cm data. This discrepancy cannot be resolved by introducing SO_2(g) into the solution since its absorptivity is more comparable to that of H_2SO_4(g) at 3.6 cm than at 13 cm (i.e., negative amounts of SO_2(g) would be required to reconcile the discrepancy). Since the experimental uncertainties in the laboratory data which furnished (12) are much greater at 3.6 cm than at 13 cm, it seems reasonable to perturb the most uncertain term to achieve agreement between the 13-cm and the 3.6-cm data sets. We found that adjusting the temperature dependence for 3.6 cm in (12) from -3 to -3.1 gave the best fit to the 13-cm results. This new expression predicts 3.6-cm absorptivities which

fall at the edge of the error bars for the laboratory data upon which (12) is based (Steffes 1985). Hence, we adopt the following expression for the absorptivity of sulfuric acid vapor at 3.6-cm:

$$\alpha_{H_2SO_4}(3.6\,\text{cm}) = 4.52 \times 10^{10}\, T^{-3.1}\, P^{0.85}\, q_{H_2SO_4}\,\text{dB km}^{-1}. \quad (14)$$

It is important to note that even though the contribution from SO_2(g) has been ignored in the calculation of the H_2SO_4(g) abundance profiles presented in the following section, the 13-cm data are not very sensitive to sulfur dioxide. Laboratory measurements, in conjunction with Earth-based observations, place a range of limits on the abundance of SO_2(g) below the cloud from 62 ppm (Fahd and Steffes 1992) to as high as 170 ppm (Na *et al.* 1990). Even 200 ppm of SO_2(g) does not contribute significantly to the absorptivity profiles at 13 cm. Additionally, in order to compute limits on the abundance of sulfur dioxide, we have solved (12) and (13) with the modified expression (14) simultaneously using a nonnegative least squares technique.

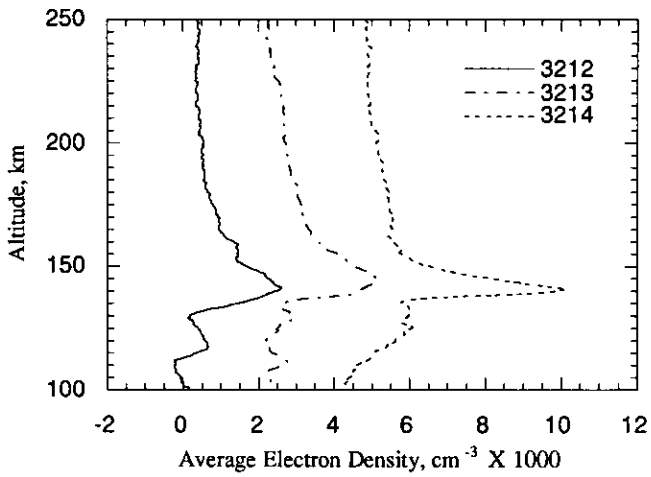

FIG. 3. Electron density profiles derived by combining the 13- and 3.6-cm frequency measurements. The profiles for orbits 3213 and 3214 have been offset by 2000 and 4000 cm^{-3}, respectively, for clarity. The results are valid to within 200 cm^{-3}. The altitude and magnitude of the main plasma peak vary significantly over the 6.5-hr period of these experiments.

3. RESULTS

The data acquired during ingress occultations on orbits 3212, 3213, and 3214 of October 5, 1991, were analyzed to infer vertical profiles of average electron density in the ionosphere; temperature, pressure, and density in the neutral atmosphere; 13- and 3.6-cm absorptivity and abundance profiles of sulfuric acid vapor; and constraints on the abundance of sulfur dioxide below the main cloud layer. The 13-cm signals probed to 33.8, 33.4, and 33.6 km on orbits 3212, 3213, and 3214, respectively (above a mean radius of 6052 km), and the 3.6-cm signals probed to 34.5, 34.3, and 35.2 km. (This compares to 40 km at 13 cm and 50 km at 3.6 cm for the Pioneer Venus Orbiter.) In addition, error bars were placed on these profiles using the standard propagation of errors (Brandt 1963). Numerical simulations with analytical models for the Venus atmosphere were conducted to validate the processing described in Section 2, Data Analysis, and to confirm the magnitude of the error bars placed on the profiles. The major features of the resulting profiles from these experiments are summarized below.

Figure 3 shows the electron density profiles obtained for each orbit. These profiles exhibit main peaks at 141, 145, and 140 km, respectively, for orbits 3212, 3213, and 3214. The altitudes of the peaks are consistent with Pioneer Venus observations (Brace *et al.* 1983). The magnitudes of the peaks, 2500, 3000, and 6000 cm^{-3}, however, are much lower than the peak of 10,000 cm^{-3} observed in 1979 during the first season of Pioneer Venus Orbiter radio occultations at the same solar zenith angle (approximately 107°), at nearly the same time in the solar cycle. Over the course of the observations, the main peak of the electron density profile increased by a factor of 2 and shifted its position vertically. The ionosphere probed by orbit 3214 also appears to be more extended than in the first two experiments, but with a narrower main plasma layer. The differences in the three profiles are highly significant, well above the estimated errors in the retrieved profiles (approximately 200 cm^{-3}). The cause for the variability in the location and magnitude of the plasma peak is unclear. If planetary scale waves or gravity waves are able to reach the ionosphere, they might be responsible for these variations in the distribution of the plasma.

Figure 4 shows the temperature profile derived from the 13-cm data for orbit 3213 along with associated uncertainties. (The 3.6-cm data sets yield the same thermal profiles to within the estimated uncertainties but do not extend as deeply as the 13-cm profiles.) The standard deviations shown in Fig. 4 include an assumed 20 K uncertainty in the boundary temperature in addition to the contributions from thermal noise. The boundary error term, however, decays rapidly, and contributes less than 10% of the standard deviation below 87 km. The temperature profiles for orbits 3213 and 3214 are similar to that for 3212, but there are significant differences in small-scale structure from orbit to orbit. Most of these differences would not be visible on the scale for this plot, had all three orbits been plotted. The temperature profile measured by the Pioneer Venus North probe at 59.7°N (Seiff *et al.* 1980) is also shown in Fig. 4. In general, the two profiles

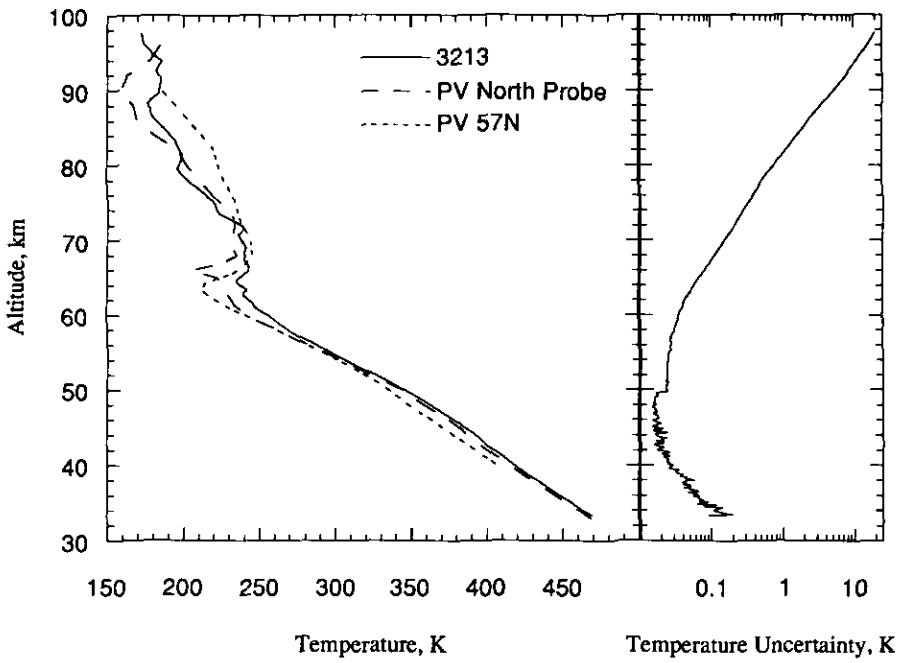

FIG. 4. Temperature profile derived from the 13-cm radio occultation experiment conducted on orbit 3213 (67°N, 113° solar zenith angle, 22:05 LTST), along with associated uncertainties (on right). Pioneer Venus North probe measurements are plotted for comparison (1978, 59.3°N, 108° solar zenith angle, 3:35 LTST). There is good agreement between the two profiles in general character, although the small-scale structure is significantly different. The 5 K discrepancy below 65 km between the two profiles is reduced if they are plotted on their respective pressure scales. The temperature profile retrieved from Pioneer Venus Orbiter orbit 57 entry radio occultation is shown as well (1979, 67.2°N, 117° solar zenith angle, 23:39 LTST). PV 57N data courtesy of A. J. Kliore (JPL).

agree with each other, although the small-scale structures are quite different and the North probe measurements were about 5 K warmer than 3212 below 65 km. This difference can also be characterized as an altitude offset of about 500 m. Plotting these two profiles on their respective pressure scales reduces this discrepancy. For reference, the pressure profile derived for orbit 3213 is plotted versus altitude in Fig. 5.

These temperature profiles are also generally similar to results from Pioneer Venus (PV) radio occultations (Kliore and Patel 1982). It is interesting to note, however, that the occultation measurements from 1978–1981 revealed a "cold polar collar," which appears as a minimum in the pressure–latitude cross section of temperature centered near 100 mbar (60–65 km altitude) and 65–70°N latitude (see Fig. 5 of Newman *et al.* 1984). The temperature profile retrieved from the Pioneer Venus orbit 57 entry occultation is also shown in Fig. 4, as an example. The reduction in temperature at this pressure level relative to the equator was as large as 40 K in the earlier measurements. Individual temperature profiles that sliced through the collar exhibit a strong temperature inversion (up to 30 K) at about 65 km altitude overlying a deep temperature minimum (~210 K) near 62 km (see Fig. 2 of Kliore and Patel 1982). This thermal feature is related to a mid-latitude jet in the zonal circulation (Newman *et al.* 1984). The absence of the cold collar in the results reported here (near 67°N) confirms the variability of this feature, which was noted in connection with the PV occultation measurements (Newman *et al.* 1984, Walterscheid *et al.* 1985),

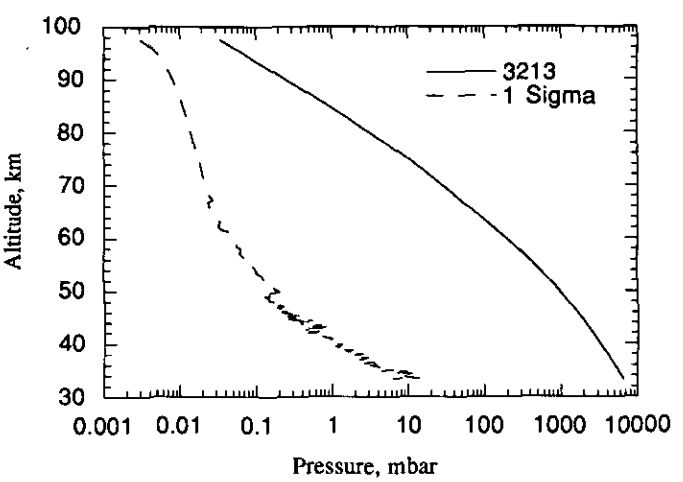

FIG. 5. Pressure versus altitude for orbit 3213 derived from the 13-cm data. The three pressure profiles derived from these measurements were nearly equal.

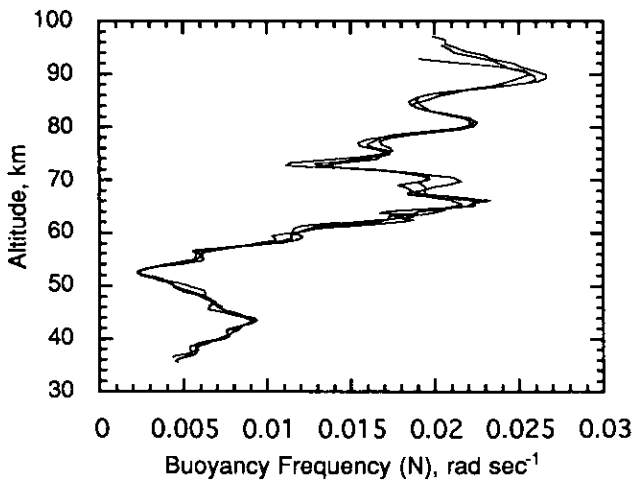

FIG. 6. Buoyancy frequency computed from the thermal structure for orbit 3213 in Fig. 4 and for orbits 3212 and 3214 (see Eq. (15)). Profiles have been smoothed to a vertical resolution of 2.4 km.

and suggests that the jet may have weakened or shifted in latitude during the past decade.

The buoyancy (or Brunt–Väiläsä) frequency, N, provides a convenient measure of atmospheric stability, where

$$N \equiv \left[\frac{g}{T}\left(\frac{dT}{dz} - \Gamma\right)\right]^{1/2}. \tag{15}$$

Here, z is the geometric height, g is the acceleration due to gravity, and Γ is the adiabatic temperature gradient. This parameter also characterizes the influence of the background thermal structure on the propagation of atmospheric waves (Andrews *et al.* 1987). Figure 6 shows vertical profiles of N, which we computed from the temperature profiles using values for Γ from Fig. 18 of Seiff *et al.* (1980). These measurements are generally consistent with previous results (e.g., Fig. 7 of Schubert 1983). The atmosphere is stably stratified at high altitudes as indicated by the relatively large values of N. The degree of stability decreases at altitudes below 65 km, reaching a minimum within the middle cloud layer (50–55 km) where the measured temperature gradient is nearly adiabatic and N approaches zero. A region of greater stability is present below the middle cloud, with N attaining a local maximum of about 10^{-2} rad/sec near 44 km altitude. Note that the temperature oscillations evident in Fig. 4 cause strong modulation of N that is highly correlated among the three profiles.

The temperature profiles derived for all three orbits exhibit statistically significant, wavelike temperature fluctuations throughout the vertical range of the measurements. The temperature variations are smallest (a few 10ths of a K) near the middle cloud layer (50–55 km) where the static stability is low. Larger amplitudes (1–5 K) are observed in regions of higher stability (near 45 km and above 60 km). Because of their relatively small amplitude, these temperature fluctuations are not fully evident in Fig. 4. There appears to be a significant degree of correlation among the temperature fluctuations in the three profiles, but differences exceeding measurement uncertainties are present as well, confirming the presence of atmospheric dynamics. Efforts toward analyzing and modeling this aspect of the data are continuing and will be the subject of forthcoming publications.

Figure 7 shows the 13- and 3.6-cm absorptivity profiles, along with their associated error bars (1σ). The absorptivity profiles show no significant absorption above 50 km, with peak absorptivities between 0.004 and 0.006 dB/km at 13 cm, and between 0.025 and 0.040 dB/km at 3.6 cm. The absorptivities include the contributions from all species, including CO_2, H_2SO_4(g), and SO_2(g).

The low uncertainties in the absorptivity profiles deserve some comment. Their low magnitudes are due to the capabilities of the Magellan spacecraft, as well as to the application of new signal processing methods. However, the magnitudes of the errors within 2 km of the base and the top of each of these profiles are understated by the standard propagation of errors. Numerical simulations have shown that the accuracy of all methods for computing numerical derivatives suffers at the edges of finite data sets. This is principally due to the two-sided nature of the definition of the derivative, which forces one to extend finite data sets artificially to estimate the derivative near the endpoints.

We feel, however, that the error bars 2 km and above the base of the profiles have been estimated conservatively. The stated uncertainties in absorptivity include an inflation factor (in the range of 30 to 50) designed to account for power fluctuations caused by small-scale refractive irregularities. In the limit of geometric optics it is possible to remove the large wavelength effects through estimation of refractive defocussing from the ray path parameters. The small wavelength structures, however, occur on a scale at which geometric optics do not apply, so that it is not possible to remove all the intensity scintillations by models based on geometric optics. In addition, the frequency estimates are corrupted by measurement noise, which forces the application of some type of filtering before the derivative in (10) is computed. The removal of some actual signal energy by the filtering step is unavoidable, especially deep in the occultation where the noise is stronger. The residual fluctuations on the excess attenuation profile are on the order of 0.1 to 1 dB and are quasi-periodic. These fluctuations are removed to a large extent by the filtering applied in the process of obtaining the absorptivity profiles. We chose to treat these residual

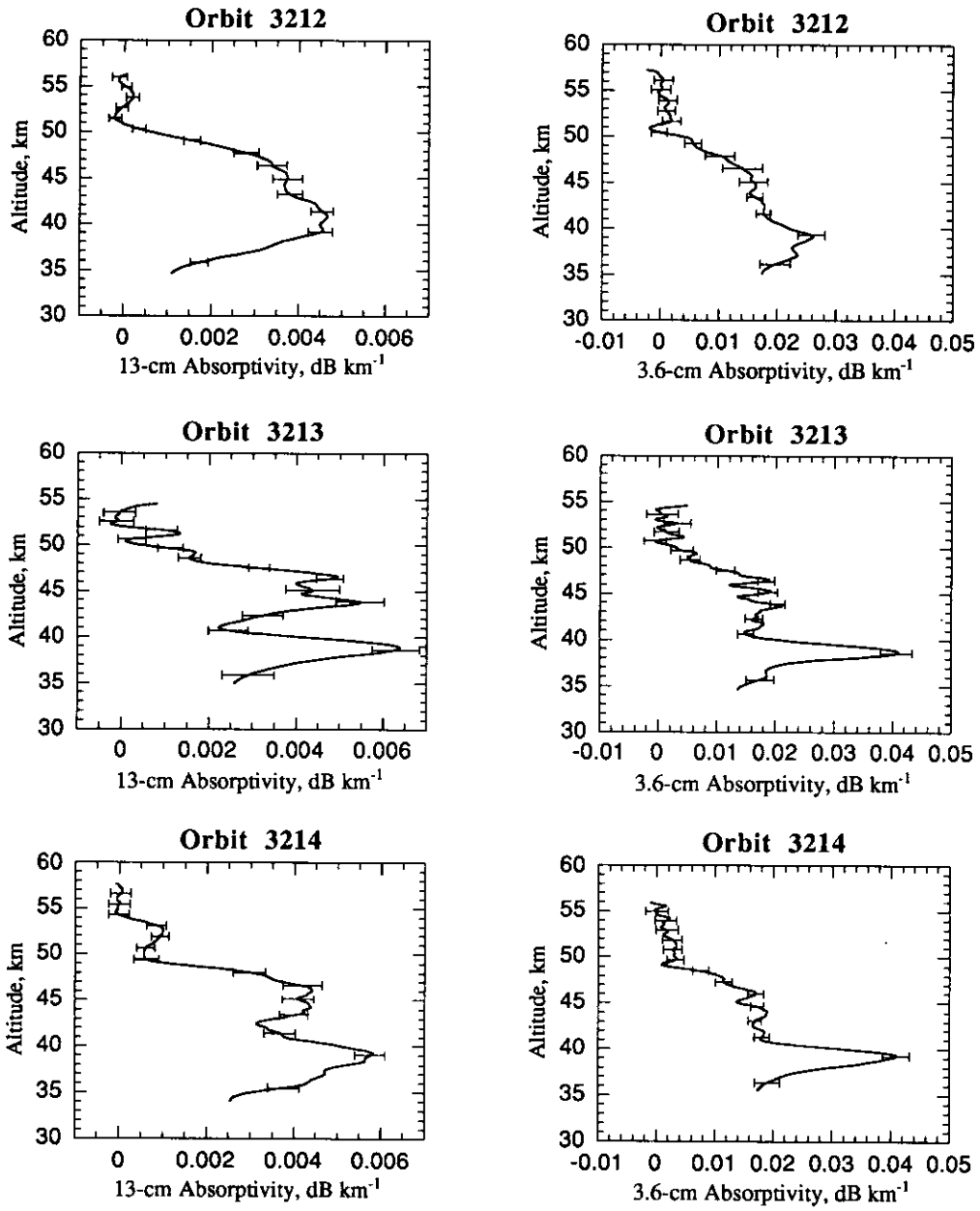

FIG. 7. Absorptivity profiles derived from the radio occultation experiment conducted on orbits 3212, 3213, and 3214, along with associated uncertainties. The 13-cm profiles are plotted on the left-hand side, the 3.6-cm profiles on the right. The accuracy of the profile improves rapidly away from the top and bottom boundaries. The results should be viewed with caution within 2 km of each boundary. These profiles result from the combined effects of CO_2, SO_2, and H_2SO_4(g).

fluctuations as white noise, and scaled the covariance matrices associated with the excess attenuation accordingly. Since the fluctuations are confined to a narrow range of the frequency domain, and are largely removed by filtering, we feel that this procedure might overestimate the errors by propagating energy at low frequencies assigned to these fluctuations through the ensuing processing. It may be possible to study the effect of such fluctuations on the derived absorptivity profiles with more sophisticated numerical simulations and to develop better methods for dealing with the errors introduced into the absorptivity profiles by the scintillations.

The abundance of H_2SO_4(g) derived from the 13-cm absorptivity profiles is shown in Fig. 8, along with the saturation abundance, and associated standard deviations. The standard deviations do not include contributions from the uncertainties in temperature and pressure, since these are insignificant compared to the uncertainties

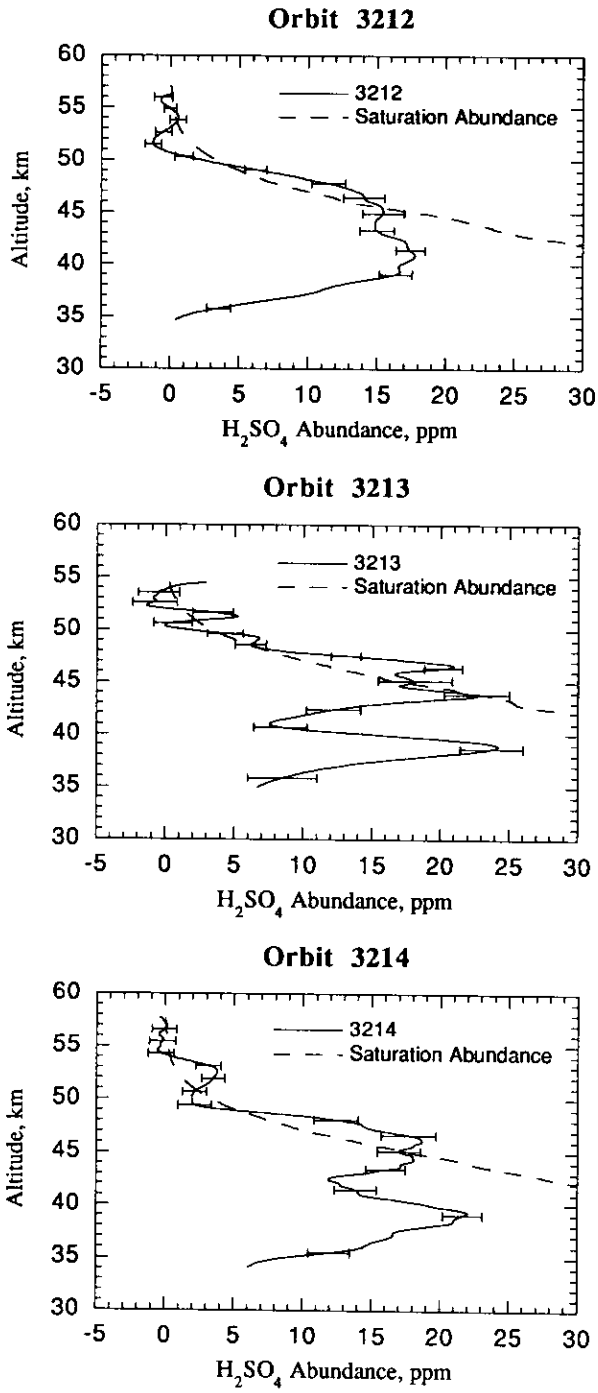

FIG. 8. Sulfuric acid vapor (H_2SO_4) abundance profiles derived from the 13-cm radio occultation experiments, along with associated uncertainties, and saturation abundance. The accuracy of the profile improves rapidly away from the top and bottom boundaries. The results should be reviewed with caution within 2 km of each boundary.

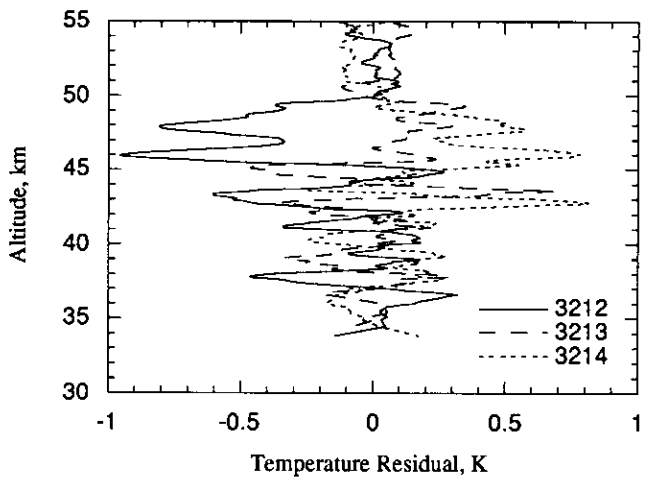

FIG. 9. Residual temperature profiles obtained by removing the average of all three profiles from each single profile. The profile for orbit 3212 is 0.5 to 1.5 K cooler than the other two between 42 and 50 km. This echoes the relationship between the three H_2SO_4(g) abundance profiles of Fig. 8, suggesting that the same dynamical process is responsible for the orbit to orbit variations in temperature and in H_2SO_4(g) abundance.

in absorptivity. Nor do they include the uncertainties in the expressions for absorptivity due to sulfuric acid vapor developed from laboratory experiments. We believe that the abundance profiles inferred from the 13-cm absorptivity profiles are more reliable than the ones derived from the 3.6-cm measurements. This is due to the additional problems associated with correcting for the antenna pointing errors at 3.6 cm and the lower uncertainties in the expression for H_2SO_4(g) absorptivity at 13 cm developed from laboratory measurements (Steffes 1985). All profiles seem to be supersaturated between 45 and 50 km, but this may be accounted for by uncertainties in the saturation abundance of H_2SO_4(g) and the mitigating presence of SO_2(g), which is not included in this analysis. Peak abundances for the sulfuric acid vapor lie between 18 and 24 ppm. The profiles decay rapidly below 38 km. The results for orbits 3213 and 3214 show a marked decrease in $q_{H_2SO_4}$ between 40 and 43 km and a strong secondary peak near 39 km, unlike orbit 3212. The differences among the profiles from the three orbits are statistically significant at some altitudes, which indicates the presence of significant variations in the small-scale structure of the abundance of sulfuric acid vapor between 34 and 50 km in the Venus atmosphere. The fact that all three abundance profiles decay below 38 km is confirmation that sulfuric acid vapor decomposes below this altitude, as it must (von Zahn *et al.* 1983).

Figure 9 shows the result of removing the average of all three temperature profiles developed for orbits 3212, 3213, and 3214 from each individual profile. This figure demonstrates that the temperature profile for 3212 is about 0.5–1.5 K cooler than those for 3213 and 3214 between 42 and 50 km. Above and below this range, the profiles overlap, although the fluctuations in the 3212 profile ap-

pear to be out of phase with those for 3213 and 3214 below 42 km. The residual temperature profiles for 3213 and 3214 bear a strong resemblance to each other and are quite different from 3212 in this region. Hence the contrast between H_2SO_4(g) abundance profile for 3212 and those for 3213 and 3214 is echoed in the temperature profiles. Although the largest difference in temperatures is from 45–50 km, while the biggest difference in H_2SO_4(g) abundance profiles is below 45 km, both may be related to the abundance and distribution of the particles in the lower cloud deck. The temperatures for 3213 and 3214 may be responding the presence of cloud particles which warm their immediate surroundings. The sulfuric acid vapor abundances may be responding to varying abundances of these particles, and to varying degrees of mixing with the atmosphere below the clouds. This leads us to suggest that the orbit to orbit variations exhibited in these thermal and abundance profiles may be caused by a common dynamical mechanism which modulates the abundance and distribution of cloud particles in the lower deck. The nature of the cause is unknown, but may be elucidated by further analysis of wave structures in the small-scale temperature fluctuations and signal intensity scintillations.

As noted in the Section 2, we had hoped to combine the 13 and 3.6-cm absorptivity measurements in order to derive SO_2(g) abundance profiles as well as H_2SO_4(g) abundance profiles. This was not possible due to the uncertainties in the expression for 3.6-cm absorptivity for sulfuric acid vapor and the inconsistencies (12) yielded. It is instructive to solve simultaneously for q_{SO_2} and $q_{H_2SO_4}$ from (12), modified as per (14), along with (13), to see what possible range of values q_{SO_2} can attain, and to illustrate the insensitivity of $q_{H_2SO_4}$ to q_{SO_2} for these types of measurements. The abundance of SO_2(g) and H_2SO_4(g) derived for orbit 3212 are presented in Fig. 10, along with representative error bars. The abundance of H_2SO_4(g) estimated by this method is consistent with the results obtained assuming no SO_2(g) is present and is basically a weighted average of the 13-cm result and the 3.6-cm result at all altitudes that the SO_2 abundance is estimated to be zero. Since the technique used to produce these solutions is nonlinear, we computed upper and lower limits by perturbing the 13- and 3.6-cm absorptivity profiles by one standard deviation and examining the resulting profiles, rather than by standard propagation of errors. The lower bound on q_{SO_2} is 0 ppm at all altitudes, but the measurement shows two regions, between 44 and 48 km and between 34 and 40 km, where q_{SO_2} is estimated to be approximately 50 ppm, with an upper bound of 200 ppm for the upper region and 150 ppm for the lower region. This would furnish an average of 31 ppm for SO_2(g) between 34 and 50 km, with a lower limit of 0 ppm and an upper limit of 139 ppm for this average. These numbers are consistent with current estimates for the average abundance of sulfur

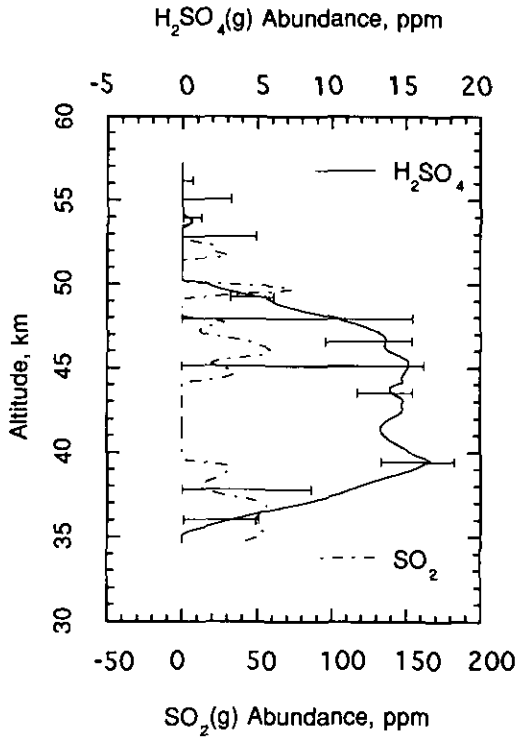

FIG. 10. Profiles of H_2SO_4(g) abundance and SO_2(g) abundance developed simultaneously from 13- and 3.6-cm absorptivity profiles from orbit 3212. The accuracy of these profiles is dependent on the validity of the temperature dependence we have chosen for the absorptivity due to H_2SO_4(g), which is open to question. This demonstrates the insensitivity of the abundance of H_2SO_4(g) derived from these measurements on the abundance of SO_2(g) present in the Venus atmosphere. It also illustrates the extent to which interpretation of dual-frequency radio occultations at Venus can be taken, if reliable expressions for the absorptivity of H_2SO_4(g) is known: retrieving independent abundance profiles of these two important sulfur-bearing gases.

dioxide below the clouds. It is not surprising that q_{SO_2} is estimated to be zero over several altitude regions since the temperature dependence assumed for the 3.6-cm H_2SO_4(g) absorptivity forces the differences between $q_{H_2SO_4}$ derived from both the 13-cm and the 3.6-cm data sets to be minimized when no SO_2(g) is assumed to be present. Any realistic theory would force the estimates derived from the 3.6-cm data in this manner to be bounded below by the 13-cm estimates. Hopefully, future laboratory measurements will yield better models for H_2SO_4(g) absorptivity that will allow the results from dual-frequency radio occultation experiments at Venus to be exploited to their full potential.

4. CONCLUSIONS AND SUGGESTIONS FOR FUTURE WORK

The three radio occultation measurements conducted on October 5, 1991, with the Magellan spacecraft provide

the most accurate, high-resolution profiles of the Venus atmosphere derived from radio occultation experiments to date. These data products include profiles of electron density, temperature, pressure, density, 13- and 3.6-cm absorptivity, and abundance of H_2SO_4(g). The small uncertainties on the thermal, absorptivity, and abundance profiles as compared with radio occultation experiments with other spacecraft are due to the higher EIRP of Magellan's HGA and recently developed signal processing methods. However, the limitations of present knowledge of absorptivity due to H_2SO_4(g) under simulated Venus conditions make it difficult to derive reliable profiles of SO_2(g) from these measurements. Based on the current state of knowledge of the microwave properties of sulfuric acid vapor, the average abundance of SO_2(g) below the clouds is 31^{+108}_{-31}. Better laboratory measurements, coupled with more advanced theories for the microwave absorptivity of H_2SO_4(g) should allow profiles of the abundance of sulfur dioxide to be developed from these and future dual-frequency radio occultation data sets.

To date, nine dual-frequency radio occultation experiments have been conducted at Venus with the Magellan spacecraft. A study of atmospheric waves based on the 1991 measurements is nearing completion and will be published separately. Processing and analysis of the six data sets obtained in December 1992 is ongoing and will be reported in future publications. Additional opportunities to conduct radio occultations of the Venus atmosphere with Magellan occur from April into October 1994. A carefully planned series of occultation experiments would provide information on the global distribution of H_2SO_4(g) and potentially, SO_2(g), as well as valuable information regarding atmospheric dynamics. Finally, a series of near-equatorial radio occultation experiments conducted in conjunction with Earth-based near infrared imaging at 2.36 μm, might elucidate the identities of the large particles responsible for large dark features that have been previously detected and tracked (Ragent *et al.* 1991, Jenkins and Ragent 1992).

APPENDIX A

Solution of the Two-Way Radio Occultation Problem

As described in Section 2 the processing of radio occultation data to yield refractivity or absorptivity profiles requires solving for the ray path parameters given the frequency received at the ground station as a function of time. This appendix describes a novel method for solving the two-way occultation problem without placing artificial constraints on the solution. This method will be referred to as the Iterated Two-Way method. For this discussion all positions and velocities relevant to the occultation geometry are assumed to be known exactly. In addition, it is assumed that the refractivity is a spherically symmetric function, and that the spatial scale of variations in refractivity is large compared to the Fresnel scale, so that geometric optics adequately describes the amplitudes and frequencies of the signals received at the ground station.

Figure 2 illustrates the geometry for one leg of a two-way occultation experiment. The vectors $\mathbf{p}_E$ and $\mathbf{P}_{SC}$ are the positions of the Earth station and the spacecraft relative to the center of Venus at the relevant times, with corresponding velocities $\boldsymbol{\nu}_E$ and $\boldsymbol{\nu}_{SC}$. The vectors $\hat{x}_1$, $\hat{x}_2$ are unit vectors defining the free-space ray asymptotes, and $\hat{x}_3$ defines the "line of sight" between the Earth station and the spacecraft for a particular link. The superscripts "+" and "−" will be used to denote uplink parameters and downlink parameters, respectively. Consider the signal received at time t_i at the Earth station. The path along which this signal traveled began at $t_i - 1/c\,(R^-_{E\_SC} + R^+_{E\_SC})$, where c is the speed of light and $R^+_{E\_SC}$ and $R^-_{E\_SC}$ are the uplink and downlink distances from the Earth station to the spacecraft. The uplink ray path carried it through the atmosphere, bending it by an angle of δ^+, with ray asymptotes a^+ km from the planet. The spacecraft received the signal and radiated a signal with a frequency 240/221 times the frequency of the signal it received. The downlink ray traversed the atmosphere once again, bending by δ^-, with a ray impact parameter of a^-. These ray path parameters are also defined by the angles $\theta^\pm_1$ and $\theta^\pm_2$. Since the refractivity of the atmosphere is a radial function, these two ray paths are constrained to lie in planes containing the Earth station (at transmission or reception), the center of Venus, and the spacecraft (cf. Born and Wolf 1965). Assuming that the units of velocity are in the speed of light and all positions and velocities are with respect to Venus, the frequency received at the ground station at time t_j is given by

$$f_r = f_t G^+ \left(\frac{1 - \boldsymbol{\nu}^+_S \cdot \hat{x}^+_2}{1 - \boldsymbol{\nu}^+_E \cdot \hat{x}^+_1}\right) \frac{240}{221} G^- \left(\frac{1 + \boldsymbol{\nu}^-_E \cdot \hat{x}^-_1}{1 + \boldsymbol{\nu}^-_S \cdot \hat{x}^-_2}\right), \tag{A1}$$

where f_r is the frequency of the reference signal uplinked to the spacecraft, $\boldsymbol{\nu}^\pm_E$ is the velocity of the Earth station at the time the reference signal left the Earth station, and $\boldsymbol{\nu}^+_{sc}$ and $\boldsymbol{\nu}^-_{sc}$ are the position and velocity of the spacecraft at the time the uplink signal reached the spacecraft (in the uplink and downlink occultation planes, respectively, which are different), $\boldsymbol{\nu}^-_E$ is the velocity of the Earth station at time t_i, and G^+ and G^- are relativistic terms in the Doppler shift on uplink and downlink, respectively. Spherical symmetry constrains the ray asymptotes $\hat{x}_1$ and $\hat{x}_2$ to pass the same distance from Venus:

$$\|\mathbf{p}^+_E - (\mathbf{p}^+_E \cdot \hat{x}^+_1)\hat{x}^+_1\| = \|\mathbf{p}^+_{SC} - (\mathbf{p}^+_{SC} \cdot \hat{x}^+_2)\hat{x}^+_2\| \tag{A2}$$

and

$$\|\mathbf{p}^-_E - (\mathbf{p}^-_E \cdot \hat{x}^-_1)\hat{x}^-_1\| = \|\mathbf{p}^-_{SC} - (\mathbf{p}^-_{SC} \cdot \hat{x}^-_2)\hat{x}^-_2\|. \tag{A3}$$

Thus, at each point in time, we have three equations and four unknowns (the directions of the ray asymptotes), which is an underdetermined set of equations for which no unique solution exists.

Lipa and Tyler (1979) describe three methods for solving these equations:

1. The Parallel Ray approximation method: Assume that the uplink ray and the downlink ray are parallel in the vicinity of the Earth station: $\hat{x}^+_1 \cdot \hat{x}^+_3 = \hat{x}^-_1 \cdot \hat{x}^-_3$. (Lipa and Tyler considered the constraint $\hat{x}^+_1 = \hat{x}^-_1$. We note that in the absence of an atmosphere, this does not allow the rays to travel along the line-of-sight paths, which is not desirable.) The ray path parameters must be solved for iteratively using this method at each time step.

2. The Mean Earth approximation method: Assume that the uplink and downlink ray paths are the same. The position and velocity of the ground station at both uplink and downlink are taken to be the position and velocity of the ground station at the time that the spacecraft received the signal uplinked from Earth, forcing $\hat{x}^+_1 = \hat{x}^-_1$ and $\hat{x}^+_2 = \hat{x}^-_2$. The ray path parameters must be solved for iteratively using this method at each

time step. A modification of this method is the Infinite Mean Earth approximation, which makes the additional assumption that Earth is an infinite distance from the spacecraft. In this case, the Doppler effects due to the motion of Earth relative to the planet are identical for the line of sight path and the actual bent path, and hence, can be canceled. This leads to a single equation that can be solved analytically.

3. Apply the Lanczos inversion iteratively to linearized versions of Eqs. (A1), (A2), and (A3). This method produces the "smallest" vector in the infinite family of solutions to an underdetermined set of linear equations (Jackson 1972).

The first two approximations reduce the number of unknowns to be equal to the number of independent equations. Solving the resulting equations does not produce the downlink ray path parameters, but rather approximations to the desired parameters which are averages of both the uplink and the downlink ray path parameters in some sense. The third method does not produce the exact downlink ray path parameters either, since it constrains the solution to be stable in a least-squares sense that may not reflect the true structure of the atmosphere.

However, the approaches considered to date have not taken into account that more information is available that can be brought to bear on the problem. We are trying to reconstruct the function $n(r)$ from the time samples $\{f(t_1), f(t_2), \ldots, f(t_N)\}$ of the function $f_r(t)$. Since $f_r(t)$ contains information about $n(r)$ down to the lowest altitude probed at time t_i it should be possible to use $\{f(t_1), f(t_2), \ldots, f(t_i)\}$ and the accompanying geometries to determine uniquely the uplink and downlink parameters at time step i. In fact, for each ray, the uplink and the downlink ray paths are determined uniquely by the refractivity $n(r)$, or equivalently, $\delta(a)$. Any solution for the downlink ray path parameters can be tested by tracing through the resulting atmospheric model $\delta(a)$ at each point i in time to determine δ_i^+, a_i^+, δ_i^-, and a_i^-, and comparing the observed frequency with the frequency predicted by this model of the atmosphere from (A1). This provides a means for testing any method for solving for the ray path parameters and also points in the direction of a better technique for solving this problem: develop an algorithm designed to drive this error function to zero.

The way to solve the problem is to define parameters that relate the uplink parameters to the downlink parameters. This would provide an additional equation, thus raising the total number of equations to the number of unknowns. One method for doing this is to make one of the methods described above to obtain a first approximation for the downlink ray path parameters. The next step is to use the occultation geometry and the approximate model $\{(a_1, \delta_1), (a_2, \delta_2), \ldots, (a_N, \delta_N)\}$ to trace through the atmosphere at each time step and determine the difference $\Delta\theta_1 \equiv \theta_1^+ - \theta_1^-$, which relates the uplink parameters to the downlink parameters. This time series of differences is used as the new constraint in solving for the ray path parameters on a point-by-point basis. The procedure is repeated until convergence is achieved. This procedure is sketched below:

1. Solve for the ray path parameters using a simplifying approximation such as the mean Earth assumption.

2. Trace through the resulting model atmosphere to estimate the difference $\Delta\theta_1$ at each time step.

3. Solve for the ray path parameters using the set of constraints $\theta_1^- = \theta_1^+ - \Delta\theta_1$.

4. Repeat steps 2 and 3 until convergence is achieved or no meaningful improvements are obtained.

In practice, thermal noise does not make is possible to use the entire set of ray path parameters as the model for the atmosphere. They must be filtered to produce well-behaved functions. Also, it is difficult to determine exactly where the top of the sensible atmosphere is. Both of these difficulties make it impossible to wait for the algorithm to converge to the point where the difference between the new solution and the old solution is identically zero. We chose to stop the algorithm when this difference behaved approximately like a zero-mean white process.

For the purposes of comparison, a synthetic data set was constructed using the occultation geometry for orbit 3212 and a model atmosphere derived from the results of orbit 3212. The WGN added to the data was chosen to model the thermal noise measured on the experiments reported here. Three methods were applied to the noise-corrupted synthetic data set for comparison: the Infinite Mean Earth approximation, the Parallel-Ray approximation, and the Iterated Two-Way method. Figure A1 shows errors in retrieved ray path parameters. The errors displayed for the Iterative Two-Way method are standard deviations. The errors displayed for the other two methods, the Infinite Mean Earth approximation and the Parallel-Ray approximation are absolute errors, and include

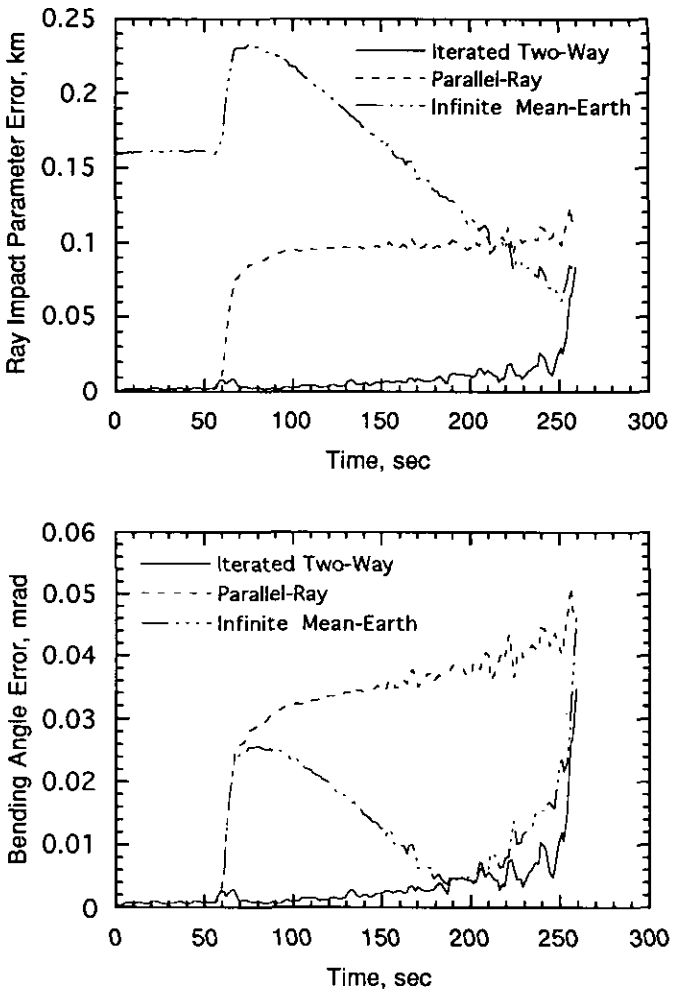

FIG. A1. Ray path parameter errors for various methods for simulated data. The errors due to the Iterated Two-Way method, the Parallel-Ray Approximation, and the Infinite Mean Earth Approximation for a synthetic data set are plotted. The curve for the Iterated method represents the envelope of statistical errors for all three methods. The errors for the other two methods are not standard deviations, but actual errors. The graph on the top displays the errors in ray impact parameter, which is related to the vertical scale retrieved for the profiles. The graph on the bottom shows the errors in bending angle, which is directly related to the temperature, pressure, and density derived from such data. The new Iterated method presented here is clearly superior to the other two methods, which introduce systematic errors that are significantly greater than statistical errors.

the combined effects of statistical errors and systematic errors. The statistical errors are nearly the same for all three methods.

Errors in Ray Path Parameter: The Infinite Mean Earth approximation yields the highest errors in ray impact parameter, up to 0.23 km. The errors due to the Parallel-Ray approximation are much smaller, starting at 0, since this approximation is exact in the absence of atmospheric bending, and rising quickly to 0.1 km once the ray path dips into the atmosphere. The errors for the Iterated Two-Way method are due entirely to the noise added to the data, and remain well below the systematic errors for either of the other two methods until the end of the experiment.

Errors in Bending Angle: The errors in retrieved bending angle are somewhat different. The Infinite Mean Earth approximation yields errors as high as 0.029 mrad, but these drop as the experiment progresses, until they reach the statistical errors plotted due to the Iterated Two-Way method. The Parallel-Ray approximation, however, yields errors in bending angle that grow monotonically from about 0.03 mrad at the edge of the atmosphere, to 0.05 mrad, where they match the statistical errors.

These results show that using one of these two "old" methods yields a strong bias in the vertical scale placed on the measurements, or a significant bias in the thermal profiles derived from the resulting ray path parameters. Although these systematic errors may be small compared to the scale of the resulting profiles, they would not be included in any error analysis based on the standard propagation of errors, which assumes that all operations performed on the data contain no systematic errors. In choosing whether or not to make use of this algorithm, the quality of the data and the experimental geometry should be taken into account.

ACKNOWLEDGMENTS

The authors extend their most heartfelt thanks to the Magellan Project for conducting these experiments and making the data available to the community. We note especially the efforts of Project Scientist, R. S. Saunders; Project Manager, D. G. Griffith; Project Engineer, D. K. Okerson; and most especially Science Manager, T. W. Thompson. We are deeply grateful to the Jet Propulsion Laboratory (JPL) project personnel and the JPL Multimission Radioscience Support Team who helped in this effort, including D. Lyons, G. M. Gonzales, A. Devereaux, A. Horton, A. Nakata, and the Deep Space Network operators. We thank Arvydas J. Kliore (JPL) for making the thermal profile for Pioneer Venus orbit 57N available to us in digital form. We also thank R. Simpson (Stanford University) for his assistance with the SUN workstation used to process the data. JMJ was supported under Grant NCC 2-753 from NASA Ames Research Center, Pioneer Venus Guest Investigator Program, and under the Venus Data Analysis Program. PGS was supported by Grant NAGW-533 from the NASA Planetary Atmospheres Program. JDT was supported by NASA under Contract JPL 957625 from the Mars Observer Project. GLT was supported by NASA under Contract JPL 957089 from the Magellan Project. DPH was supported under Grant NAGW-3443 of the Venus Data Analysis Program.

REFERENCES

ANDERSSEN, R. S. 1976. Stable procedures for the inversion of Abel's equation. *J. Inst. Math. Appl.* **17,** 329–342.

ANDERSSEN, R. S., AND P. BLOOMFIELD 1974a. A time series approach to numerical differentiation. *Technometrics* **16**(1), 69–75.

ANDERSSEN, R. S., AND P. BLOOMFIELD 1974b. Numerical procedures for non-exact data. *Numerische Mathematik* **22,** 157–182.

ANDREWS, D. G., J. R. HOLTON, AND C. B. LEOVY 1987. *Middle Atmosphere Dynamics*. Academic Press, Orlando.

BORN, M., AND E. WOLF 1965. *Principles of Optics*, Pergamon, New York.

BRACE, L. H., H. A. TAYLOR, JR., T. I. GOMBOSI, A. J. KLIORE, W. C. KNUDSEN, AND A. F. NAGY 1983. The ionosphere of Venus: Observations and their interpretations. In *Venus* (Hunten, Colin, Donahue, and Moroz, Eds.), pp. 779–840. Univ. of Arizona Press, Tucson.

BRACEWELL, R. N. 1986. *The Fourier Transform and its Applications*, 2nd ed. pp. 262–266. McGraw-Hill, New York.

BRANDT, S. 1963. *Statistical and Computational Methods in Data Analysis*. North-Holland, Amsterdam.

ESSEN, L., AND K. D. FROOME 1951. The refractive indices and dielectric constants of air and its principle constituents at 24000 Mc/s, *Proc. Phys. London B* **64,** 862–875.

ESHLEMAN, V. R. 1973. The radio occultation method for study of planetary atmospheres. *Planet. Sci.* **21,** 1521–1531.

ESHLEMAN, V. R., D. O. MUHLEMAN, P. D. NICHOLSON, AND P. G. STEFFES 1980. Comment on absorbing regions in the atmosphere of Venus as measured by radio occultations. *Icarus* **44,** 793–803.

FAHD, A. K., AND P. G. STEFFES 1992. Laboratory measurements of the microwave and millimeter-wave opacity of gaseous sulfur dioxide (SO_2) under simulated conditions for the Venus atmosphere. *Icarus* **97,** 200–210.

FJELDBO, G., AND V. R. ESHLEMAN 1968. The atmosphere of Mars analyzed by integral inversion of the Mariner IV occultation data. *Planet. Space Sci.* **16,** 1035–1059.

FJELDBO, G., A. J. KLIORE, AND V. R. ESHLEMAN 1971. The neutral atmosphere of Venus as studied with the Mariner V radio occultation experiments. *Astron. J.* **76**(2), 123–140.

FURUTA, O., H. YUKI, AND M. YAMANDA 1985. Abrupt changes in cross polarizations observed during thunder. *IEEE Trans Antennas Propagation* **AP-33,** 625–632.

HO, W., I. A. KAUFMAN, AND P. THADDEUS 1966. Laboratory measurements of microwave absorption models of the atmosphere of Venus. *J. Geophys. Res.* **71,** 5091–5108.

JACKSON, D. D. 1972. Interpretation of inaccurate, insufficient and inconsistent data. *Geophys. J. R. Astron. Soc.* **28,** 97–109.

JENKINS, J. M. 1992. *Variations in the 13 cm Opacity below the Main Cloud Layer in the Atmosphere of Venus Inferred from Pioneer–Venus Radio Occultation Studies 1978–1992*. Ph.D. dissertation, Georgia Institute of Technology.

JENKINS, J. M., AND B. RAGENT 1992. Preliminary correlation of recent NIR images of Venus with Pioneer Venus Orbiter radio occultation studies. *Bull. Am. Astron. Soc.* **24,** 1002. [Presented at the 24th Annual Meeting of the DPS/AAS in Munich, Germany]

JENKINS, J. M., AND P. G. STEFFES 1991. Results for 13-cm absorptivity and H_2SO_4 abundance profiles from the Season 10 (1986) Pioneer–Venus Orbiter radio occultation experiment. *Icarus* **90,** 129–138.

KLIORE, A. J., AND I. R. PATEL 1982. Thermal structure of the atmosphere of Venus from Pioneer Venus radio occultations. *Icarus* **52,** 320–334.

LIPA, B., AND G. L. TYLER 1979. Statistical and computational uncertainties in atmospheric profiles from radio occultation: Mariner 10 at Venus. *Icarus* **39,** 192–208.

NA, C. Y., L. W. ESPOSITO, W. E. MCCLINTOCK, AND C. A. BARTH 1990. Rocket observations of Venus SO_2. *Bull. Am. Astron. Soc.* **22,** 1054. [Presented at the 22nd Annual Meeting of the DPS/AAS in Charlottesville, VA]

NEWMAN, M., G. SCHUBERT, A. J. KLIORE, AND I. R. PATEL 1984. Zonal winds in the middle atmosphere of Venus from Pioneer Venus radio occultation data. *J. Atmos. Sci.* **41,** 1901–1913.

RAGENT, B., L. TRAVIS, D. CRISP, D. ALLEN, P. STEFFES, J. JENKINS, G. DEARDORFF, AND Y. HUNG 1991. Correlation of Earth-based NIR

imagery and Pioneer–Venus Orbit imagery and data. *Bull. Am. Astron. Soc.* **23,** 1192. [Presented at the 23rd Annual Meeting of the DPS/AAS in Palo Alto, CA]

SAUNDERS, R. S. 1992. *Magellan at Venus*. Reprinted from the *J. Geophys Res.* **97,** Nos. E8 and E9.

SCHUBERT, G. 1983. General circulation and the dynamical state of the Venus atmosphere. In *Venus* (D. M. Hunten, L. Colin, T. M. Donahue, and V. I. Moroz, Eds.), pp. 681–765. Univ. of Arizona Press, Tucson.

SEIFF, A. 1983. Thermal structure of the atmosphere of Venus. In *Venus* (Hunten, Colin, Donahue, and Moroz, Ed.), pp. 215–279. Univ. of Arizona Press, Tucson.

SEIFF, A., D. B. KIRK, R. E. YOUNG, R. C. BLANCHARD, J. T. FINDLAY, G. M. KELLY, AND S. C. SOMMER 1980. Measurements of thermal structure and thermal contrasts in the atmosphere of Venus and related dynamical observations: Results from the four Pioneer Venus probes. *J. Geophys. Res.* **85,** 7903–7933.

STEFFES, P. G., AND V. R. ESHLEMAN 1982. Sulfuric acid vapor and other cloud-related gases under simulated conditions for the middle atmosphere of Venus. *Icarus* **51,** 322–333.

STEFFES, P. G. 1985. Laboratory measurements of the microwave opacity and vapor pressure of sulfuric acid under simulated conditions for the middle atmosphere of Venus. *Icarus* **64,** 576–585.

STEFFES, P. G., J. M. JENKINS, R. S. AUSTIN, S. W. ASMAR, D. LYONS, E. H. SEALE, AND G. L. TYLER 1994. Radio occultation studies of the Venus atmosphere with the Magellan spacecraft. 1. Experiment description and performance. *Icarus* **110,** 71–78.

VON ZAHN, U., S. KUMAR, H. NIEMANN, AND R. PRINN 1983. Composition of the Venus atmosphere. In *Venus* (D. M. Hunten, L. Colin, T. M. Donahue, and V. I. Moroz, Eds.), pp. 299–430. Univ. of Arizona Press, Tucson.

WALTERSCHEID, R. L., G. SCHUBERT, M. NEWMAN, AND A. J. KLIORE 1985. Zonal winds and the angular momentum balance of Venus' atmosphere within and above the clouds. *J. Atmos. Sci.* **42,** 1982–1990.